Neutron and photon production from thick targets bombarded by 30-MeV p, 33-MeV d, 65-MeV ^{3}He, and 65-MeV α ions: Experiment and comparison with cascade Monte Carlo calculations

Kazuo Shin, Kouki Hibi,* and Masahiko Fujii†
Department of Nuclear Engineering, Kyoto University, Yoshida-Honmachi, Sakyo-ku, Kyoto, Japan

Yoshitomo Uwamino and Takashi Nakamura
Institute for Nuclear Study, University of Tokyo, Midori-cho, 3-2-1, Tanashi, Tokyo, Japan
(Received 8 November 1983)

The energy spectra of neutrons and photons emitted by thick targets of carbon, iron, copper, and lead at angles of 0, 15, 30, 45, 75, and 135 deg to the incident beam of 33-MeV deuteron, 65-MeV ^{3}He, and 65-MeV alpha ions were obtained by unfolding the pulse height distributions measured with an NE-213 scintillator. The angular distributions of neutrons above 4 MeV and photons above 1.5 MeV were obtained by integrating the measured spectra. The total neutron yield was obtained by estimating the neutron yield below a few MeV by fitting the spectra measured above that energy to the Maxwellian distribution and showed good agreement with other experimental results. The measured spectra were analyzed by the thick-target radiation transport Monte Carlo code based on the intranuclear-cascade-evaporation model. The validity of the model was tested at the lower projectile energy limit through this comparison.

I. INTRODUCTION

The application of medium energy particle accelerators is widespread in material damage studies, particle radiation therapy, production of an intense neutron source, radioisotope production for nuclear medicine, etc. The fundamental importance of accelerator shielding has increased accordingly. For these purposes, it is necessary to get accurate detailed information on secondary neutron and photon production from various kinds of thick targets.

Much work has been done on secondary neutron production by charged particles, as is summarized in Ref. 1, but most of the data are limited to some particular projectile and target combination, such as protons and deuterons on lithium and beryllium targets. In the projectile energy below 100 MeV, there are several studies on neutron production from thick targets of other elements, by proton,[2] deuteron,[3,4] and alpha ions.[5–7] On the other hand, the only data on secondary photon production from thick targets by charged particles that have ever been reported have been by us for 52-MeV protons.[8]

We have already published a paper[9] on neutron production from thick carbon, iron, copper, and lead targets bombarded by 30- and 52-MeV protons. In that paper, our measured results of the angular-dependent neutron energy spectra, and the angular distribution of the neutron flux, were compared with those calculated with Bertini's intranuclear-cascade evaporation Monte Carlo code MECC–7.[10] In this successive study, we measured the secondary neutron and photon energy spectra emitted in several directions from thick targets of carbon, iron, copper, and lead bombarded by 33-MeV deuteron, 65-MeV ^{3}He, and 65-MeV alpha ions, and obtained angular distributions of neutron and photon fluxes and the neutron and photon yields. Our experimental results for neutrons were also analyzed by the thick-target radiation transport Monte Carlo code for low-mass heavy-ion beams, LHI.[11] This code is based on the same intranuclear-cascade-evaporation model as the MECC–7 code and is believed to be a reasonably good approximation for relatively low projectile energies ($\lesssim$10 GeV/nucleon) for ions of p, n, d, t, ^{3}He, and α, and for target nuclei of atomic mass heavier than 10. From this comparison, we tried to find the lower projectile energy limit of validity of the LHI code.

II. EXPERIMENTAL PROCEDURE

The experimental arrangement is shown in Fig. 1. Accelerated beams of 33-MeV deuterons, 65-MeV ^{3}He, and 65-MeV alpha particles from the SF cyclotron of the Institute for Nuclear Study (INS) at the University of Tokyo bombarded thick carbon, iron, copper, and lead targets fixed perpendicularly to the beam axis in a scattering chamber. The targets were 20 mm in diameter. The thickness of each target shown in Table I was selected to be a little thicker than the range of an incident particle, so that the projectile would be absorbed completely and the self-scattering and self-absorption of the neutrons and gamma rays produced would be negligible.

The secondary neutrons and photons emitted at 0, 15, 30, 45, 75, and 135 deg directions (see Table I) to the beam axis at the target were measured with a 76.2-mm-diam $\times$76.2-mm-long NE-213 scintillator placed at a point 4 m behind the target. The pulse height measurements of neutrons and photons were performed separately at the same time by using the n-γ pulse shape discrimination technique coupled with a two-dimensional multichannel

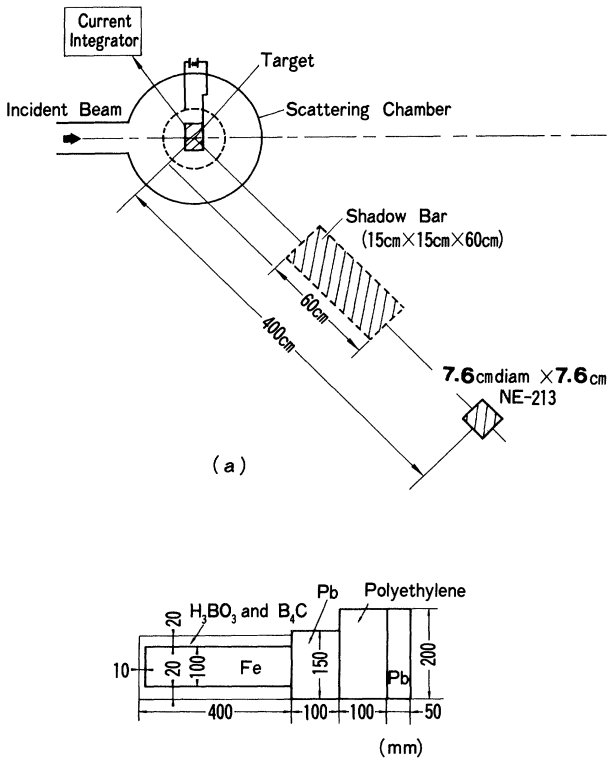

FIG. 1. Conceptual drawing of the experimental arrangement (a), and the laminated shadow shield (b).

analyzer, as shown in Fig. 2. These measurements were performed using a very weak beam intensity of about 0.1 nA for the deuterons, 0.1 ~ 1 nA for ^{3}He, and a few to approximately 20 nA for the alpha particles to avoid pulse pileup. The energy calibration of the detector was carried out with ^{60}Co gamma rays and 4.43-MeV gamma rays from an Am-Be neutron source. The pulse height output

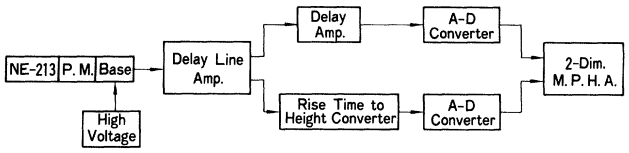

FIG. 2. Block diagram of the neutron and photon measuring system.

distributions were unfolded to obtain neutron and photon energy spectra using the revised FERDO unfolding code,[12] with the aid of response functions to neutrons calculated up to 100 MeV (Ref. 13) and to photons calculated up to 14 MeV.[14]

The FERDO code unfolds a light output distribution in the following way,

$$P = UC \,, \tag{1}$$

where P is the energy spectrum vector, C is the light output distribution vector, and U is the matrix calculated with the response functions of the detector.

The vector P has three types of errors, i.e., the statistical error of C, the error caused by the unfolding calculation truncated at the finite dimensions of the vectors and the matrix in Eq. (1), and the statistical error of the response function obtained by the Monte Carlo calculation. The revised FERDO code evaluates all three errors, including the propagation of the response function errors. All neutron and photon spectra obtained have lower limits at 2 – 4 MeV and 1.5 MeV, respectively, coming from the dynamic range of the n-γ discrimination circuit. The number of particles incident on the target was measured by the current integrator connected to the target. The target was surrounded by a – 100 V suppressor grid as shown in Fig. 1. The suppressor grid permitted an accurate determination of the number of projectiles by repelling secondary electrons backscattered from the target.

An estimation of the background contribution due to room scattering was performed by intercepting the neutrons produced at the target with a shadow bar of con-

TABLE I. Experimental conditions.

Projectile	Nuclide	Target Density (g/cm^3)	Thickness (mm)	Measuring angle (deg)
33-MeV d	C	1.7	9.0	0, 15, 45, 75, 135
	Fe	7.86	3.0	
	Cu	8.93	3.0	
	Pb	11.34	3.0	
65-MeV ^{3}He	C	1.7	9.0	0, 15, 30, 45, 75, 135
	Fe	7.86	3.0	
	Cu	8.93	3.0	
	Pb	11.34	3.0	
65-MeV α	C	1.7	6.0	0, 15, 45, 75, 135 (for C, Cu, and Pb targets) 0, 30, 45, 75, 135 (for Fe target)
	Fe	7.86	2.0	
	Cu	8.93	2.0	
	Pb	11.34	2.0	

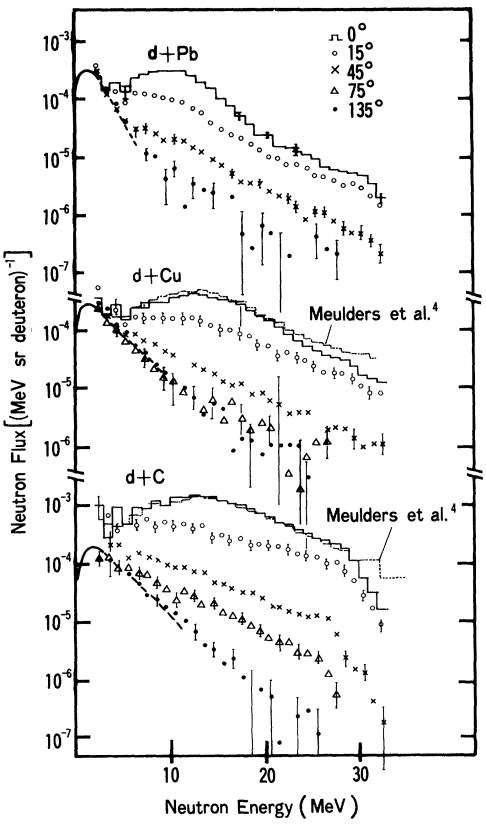

FIG. 3. Neutron spectra of carbon, copper, and lead targets for 33-MeV deuteron injection at emission angles of 0, 15, 45, 75, and 135 deg. The spectra are normalized to one incident deuteron with a standard deviation. The solid curves indicate the Maxwellian distribution fitted to the measured spectra.

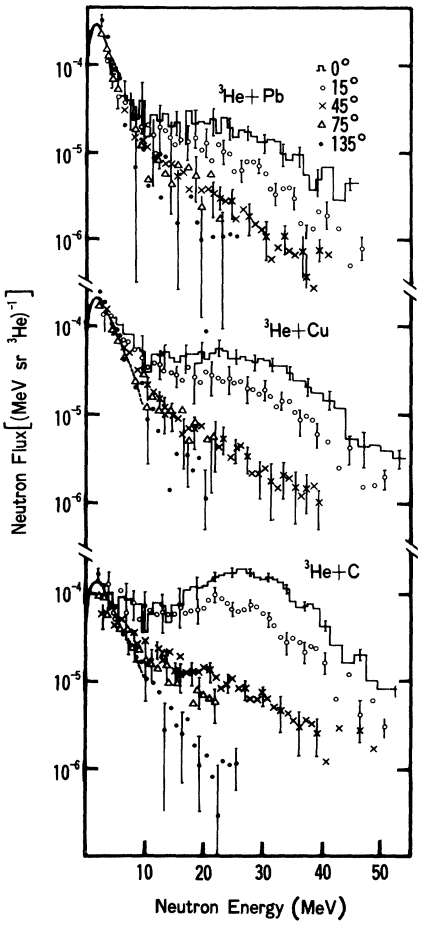

FIG. 4. Neutron spectra of carbon, copper, and lead targets for 65-MeV ^{3}He injection at emission angles of 0, 15, 45, 75, and 135 deg. The spectra are normalized to one incident ^{3}He with a standard deviation. The solid curves indicate the Maxwellian distribution fitted to the measured spectra.

crete, 15 cm wide, 15 cm high, by 60 cm long, placed between the target and the detector. To investigate whether this shadow bar is sufficient enough to shut off the direct neutrons and photons from the target, another shadow bar of laminated iron, lead, polyethylene, and lead, shown in Fig. 1(b), was also used in the case of the deuteron beam incidence. It was confirmed that both shadow bars gave the same background counts and the concrete shadow bar was quite effective to the background estimation. It was observed that the background neutrons contributed between 5% and 10% to the neutrons measured without the shadow bar, but for photons the contribution of the background was about 30—50% of the measurement without the shadow bar. The spectra reported here in this experimental geometry are corrected for this background component.

III. EXPERIMENTAL RESULTS

A. Neutron energy spectra and angular distributions

The neutron energy spectra $\phi_n(E,\theta)$ of carbon, copper, and lead targets at emission angles of $\theta=0$, 15, 45, 75, and 135 deg, normalized to one incident particle, are shown with their standard deviations for 33-MeV deuteron, 65-MeV ^{3}He, and 65-MeV alpha beams in Figs. 3, 4, and 5, respectively. The observed results for the iron target were omitted, because they are quite similar to those for the copper target.

The neutron spectra of carbon and copper targets at $\theta=0$ deg for the 33-MeV deuteron injection are compared in Fig. 3 with the results obtained by Meulders *et al.*[4] with the time-of-flight method under the same experimental conditions. The figure clearly shows that our results agree quite well both in spectral shapes and absolute values with theirs, excluding those at the high energy end. The neutron spectra in these figures indicate the following general tendencies:

(1) Except for the forward direction of the deuteron and ^{3}He beams, the neutron spectra have two components: One below about 10 MeV corresponds to neutrons produced isotropically mainly by the evaporation process; the other above 10 MeV corresponds to those produced by the direct process. Since the neutron emission by the direct process has a sharp forward peaking of the angular distribution, the neutron spectra become softer at larger emission angles, where the evaporation process is prominent.

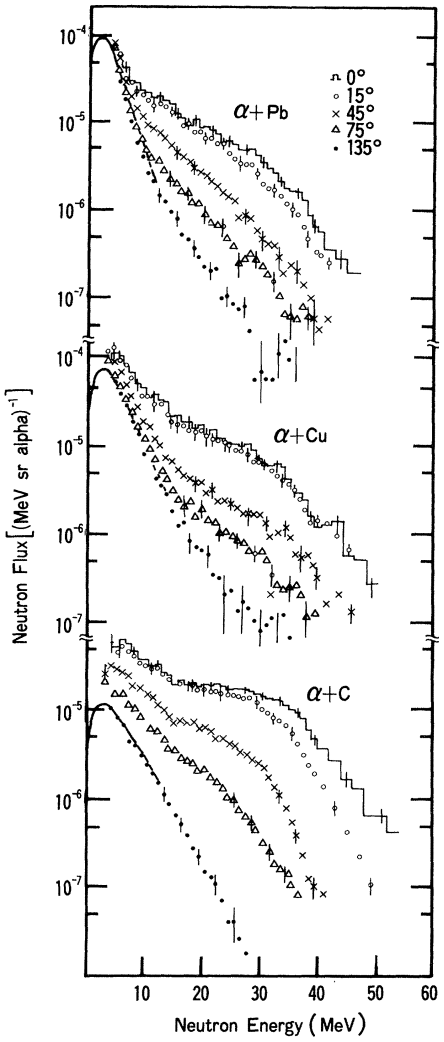

FIG. 5. Neutron spectra of carbon, copper, and lead targets for 65-MeV alpha injection at emission angles of 0, 15, 45, 75, and 135 deg. The spectra are normalized to one incident alpha with a standard deviation. The solid curves indicate the Maxwellian distribution fitted to the measured spectra.

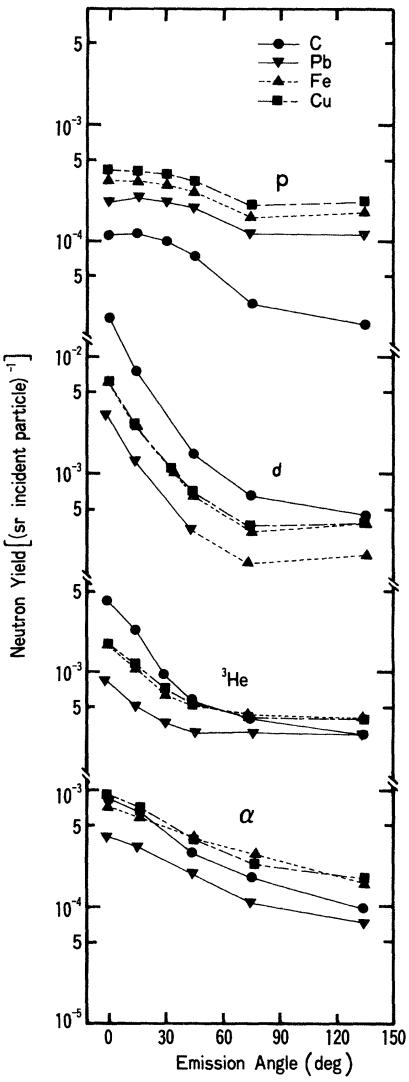

FIG. 6. Angular distributions of fast neutron fluxes integrated above 4 MeV for proton, deuteron, ^{3}He, and alpha particle incidence on carbon, iron, copper, and lead targets.

(2) In the forward direction of the deuteron and ^{3}He incidence cases, a broad peak in the neutron spectra can be clearly seen due to the stripping of the projectiles. The peak energy is about half of the incident deuteron energy and one-third of the incident ^{3}He energy.

(3) The neutron energy spectra become harder for lighter target nuclei. This can be explained by noting that the energy E_t transferred from a projectile to a target by one collision is proportional to $4M_pM_tE_0/(M_p+M_t)^2$, where M_p and M_t are the atomic masses of the projectile and target nuclei, respectively, and E_0 is the projectile kinetic energy. As a result, the sum of the transferred energies is greater for lighter target nuclei, and it is more likely that a nucleon receives a greater part of this transferred energy and that the fraction of the evaporation process is smaller, since the lighter target nucleus has a smaller number of nucleons. This implies that lighter target nuclei are excited in a state of higher nuclear temperature.

The normalized angular distributions of the neutron flux of Figs. 3—5 integrated over energy for carbon, iron, copper, and lead targets,

$$\phi_n(\theta)=\int_{E_{cut}}^{E_0}\phi_n(E,\theta)dE\ , \tag{2}$$

are shown in Fig. 6, where E_0 is the incident particle energy and E_{cut} is the lower energy bound of 4 MeV in this case. The absolute value of the neutron spectrum from deuterons on lead at 75 deg could not be given correctly; so the $\phi_n(\theta=75)$ value was estimated by the smooth interpolation of $\phi_n(\theta)$ values at other emission angles with the relevant $\phi_n(\theta)$ curves for iron and copper targets. The angular distributions of neutrons produced from 30-MeV protons[9] are also shown in the figure for comparison. Figure 6 clearly shows that the neutron angular distributions in the backward direction are almost isotropic for all projectile and target combinations, whereas in the forward direction, the forward peaking is stronger in the order of

projectile types of p, α, ^{3}He, and d, and for lighter target nuclei. This can be explained from the fact that the splitting reaction of d and ^{3}He projectiles occurs strongly in the forward direction, and that the momentum transfer from a heavier projectile to a lighter target is greater and the velocity of the center of mass is greater in the laboratory system; then based on the kinematics, a nucleon is emitted in the more forward direction from the heavier projectile and the lighter target.

B. Estimation of low energy neutron components and total neutron yield

It is very important to evaluate the neutron yield per incident particle for thick targets, together with their energy spectra and angular distributions. The fast neutron yield, i.e., the number of neutrons of energy higher than $E_{\rm cut}$, $Y_{\rm n}^{\rm fast}$, was obtained from our measured neutron spectra, $\phi_{\rm n}(E,\theta)$, as

$$Y_{\rm n}^{\rm fast}=2\pi\int_0^{\pi}\sin\theta\, d\theta\int_{E_{\rm cut}}^{E_0}\phi_{\rm n}(E,\theta)dE\ . \tag{3}$$

Table II gives the values of $Y_{\rm n}^{\rm fast}$ for $E_{\rm cut}=4$ MeV.

For practical use, it is necessary to have the total neutron yield, i.e., the number of neutrons produced over the whole energy region, $Y_{\rm n}^{\rm tot}$. Since our measured data were limited to neutron spectra above 2–4 MeV, the neutrons below that energy $E_{\rm cut}$ were evaluated in the following way. As seen in Figs. 3–5, the absolute values and the shapes of the neutron spectra in the few MeV region scarcely change with emission angle, excluding neutrons from the carbon target by d, ^{3}He, and α ions. Then, neutrons of energy lower than a few MeV can be approximated to be produced by the evaporation process having a Maxwellian energy distribution given by

$$\phi_{\rm n}(E)=C\frac{E}{\tau^2}\exp(-E/\tau)\ , \tag{4}$$

where τ is the nuclear temperature and C is a normalization constant. The values of C and τ of Eq. (4) were determined to be fitted well to the measured neutron spectra at 135 deg, and thus the values of $\phi_{\rm n}(E)$ are shown in solid curves in Figs. 3–5. This estimation of neutron evaporation is accurate enough to get the total neutron yield, although more detailed fitting is described in the following paper. For the carbon target bombarded by d, ^{3}He, and α ions, however, the contribution of neutrons produced by the nonevaporation process could still not be neglected in this low energy region in the forward direction. These nonevaporation neutron components were estimated by subtracting the $\phi_{\rm n}(E)$ value of Eq. (4) from the measured spectra $\phi_{\rm n}(E,\theta)$ for $E_{\rm cut}\leq E\lesssim\sim 10$ MeV and extrapolating the subtracted results $\phi_{\rm n}^{\rm NE}(E,\theta)$ smoothly into the energy region below $E_{\rm cut}$. The neutron energy spectra $\phi_{\rm n}'(E,\theta)$ were finally evaluated over the whole energy region as

TABLE II. Neutron and photon total yields per 100 incident particles.

Incident particle	Target	Neutron yield Experimental $Y_{\rm n}^{\rm fast\,a}$	Neutron yield Experimental $Y_{\rm n}^{\rm tot\,b}$	Neutron yield Calculation	Photon yield[c] $Y_\gamma^{\rm tot}$
30-MeV p	C	0.0503	0.130	0.986[e]	0.948
	Fe	0.259	0.938	1.04[e]	1.38
	Cu	0.320	1.33	1.27[e]	1.33
	Pb	0.176	1.64	2.81[e]	0.366
33-MeV d	C	1.75	2.64	1.51	1.68
	Fe	0.785	1.76	1.30	1.43
	Cu	0.788	1.81	1.37	1.13
	Pb[d]	0.348	1.35	1.98	0.520
65-MeV ^{3}He	C	0.650	1.21	1.45	1.39
	Fe	0.603	1.48	1.11	1.78
	Cu	0.613	1.50	1.22	1.44
	Pb	0.0404	1.56	1.43	1.03
65-MeV α	C	0.221	0.297		0.613
	Fe	0.278	0.696		0.905
	Cu	0.361	0.744		0.835
	Pb	0.162	0.531		0.413

[a]Neutron yield per 100 incident particles obtained by integrating the neutron spectrum over the energy range $E_{\rm n}\geq 4$ MeV.

[b]Neutron yield per 100 incident particles obtained by integrating the neutron spectrum over the energy range $E_{\rm n}\geq 0$ MeV.

[c]Photon yield per 100 incident particles obtained by integrating the photon spectrum over the energy range $E\geq 1.5$ MeV.

[d]Obtained using estimated values at 75 deg.

[e]Cited from Ref. 9.

$$\phi'_n(E,\theta)=\phi_n(E,\theta) \text{ in Figs. } 3-5 \text{ , for } E_{cut}\le E\le E_0 \text{ ,}$$
$$=\phi_n(E) \text{ of Eq. (4) } +\phi_n^{NE}(E,\theta) \text{ ,}$$
$$\text{for } 0\le E\le E_{cut} \text{ .} \quad (5)$$

By integrating $\phi'_n(E,\theta)$ with energy and angle, the total neutron yield, Y_n^{tot} was obtained as

$$Y_n(\theta)=\int_0^{E_0}\phi'_n(E,\theta)dE \text{ ,}$$
$$Y_n^{tot}=\int_0^{\pi}2\pi\sin\theta Y_n(\theta)dE \text{ .} \quad (6)$$

The neutron yields at 0 deg, $\phi_n(0)$ and $Y_n(0)$, obtained by Eqs. (2) and (6), respectively, for the carbon target exposed to 33-MeV deuterons, are compared with other experimental results in Fig. 7. Our result of a neutron yield above 4 MeV, $\phi_n(0)$, is in quite good agreement with that of Meulders *et al.*;[4] also our result of the total neutron yield, $Y_n(0)$, is just on the linear extrapolation in a logarithmic scale of the yield curve by Weaver *et al.*[3] For alpha ions, the total neutron yields, Y_n^{tot}, obtained by Eq. (6), for carbon and copper targets, are compared with other experimental results in Fig. 8. Figure 8 also includes the total neutron yields for 710-MeV alpha beams incident on carbon and iron targets which were estimated by Eq. (4) from the neutron angular and energy distributions measured above 3 MeV by Cecil *et al.*[15] Our results connect the total neutron yield data in the low ($\sim$10 MeV) and high energy ($\sim$700 MeV) regions well.

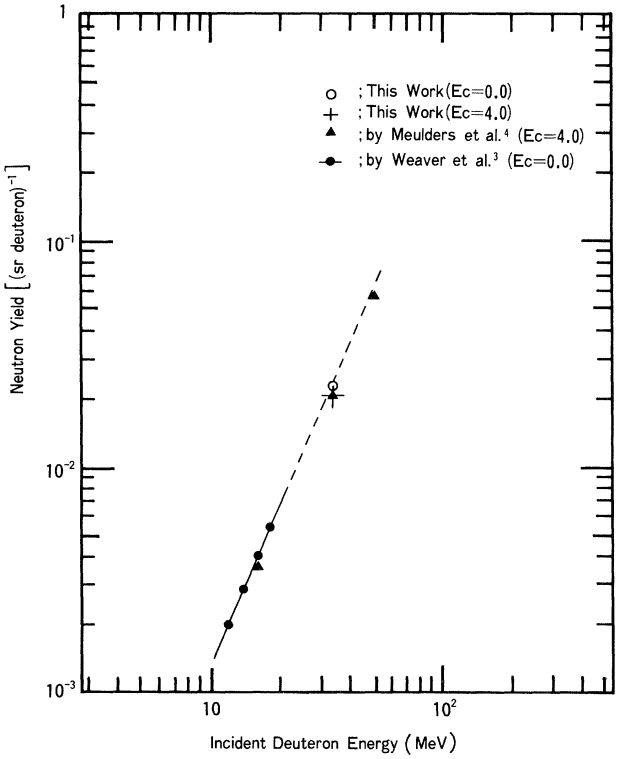

FIG. 7. Comparison of our fast ($\ge$4 MeV) and total neutron yield data at 0 deg, $\phi_n(0)$ and $Y_n(0)$, from the carbon target exposed to 33-MeV deuterons with those obtained by Meulders *et al.* (Ref. 4), $\phi_n(0)$, and Weaver *et al.* (Ref. 3), $Y_n(0)$. The dotted line shows the extrapolation of the data of Weaver *et al.* to the high energy region.

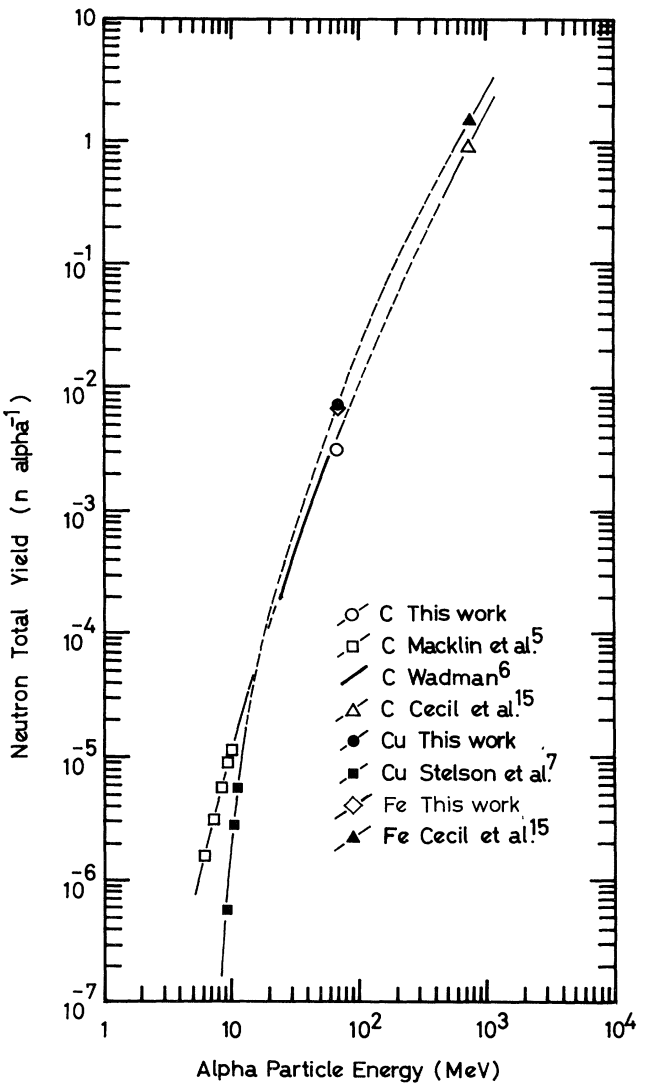

FIG. 8. Comparison of our total neutron yield data for 65-MeV alpha ions on carbon, iron, and copper targets with those by Macklin *et al.* (Ref. 5), Wadman (Ref. 6), Stelson *et al.* (Ref. 7), and Cecil *et al.* (Ref. 15). The dotted lines connect these data smoothly.

Figure 9 shows $Y_n(\theta)$ as a function of the emission angle, θ, for 30-MeV protons and 65-MeV alpha particles as examples. Compared with fast neutron angular distributions above 4 MeV, $\phi_n(\theta)$ in Fig. 6, total neutron angular distributions, $Y_n(\theta)$, become more isotropic with increasing atomic mass of the target due to the larger contribution of evaporated neutrons of energy below 4 MeV. The total neutron yields Y_n^{tot} obtained by Eq. (6) are shown in Table II. The total and fast neutron yields are the largest for the deuteron incidence on the carbon target due to a splitting reaction. As for the dependence of Y_n^{fast} on the target atomic mass M_t, Y_n^{fast} decreases with M_t for d and ^{3}He projectiles, but for p and α projectiles Y_n^{fast} increases

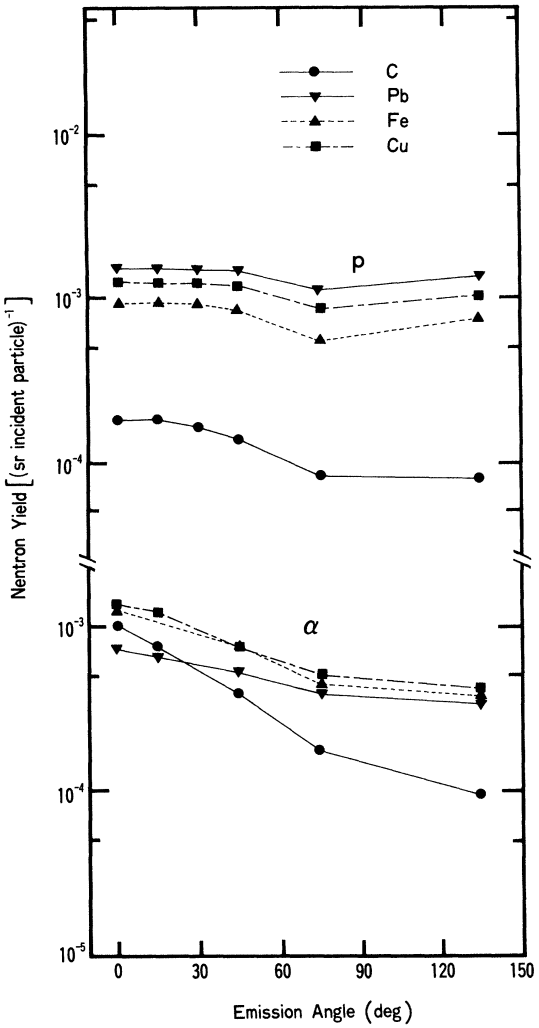

FIG. 9. Angular distributions of total neutron fluxes for 30-MeV proton and 65-MeV alpha particle incidences on carbon, iron, copper, and lead targets.

with M_t up to copper and decreases for the lead target. On the other hand, Y_n^{tot} increases montonically with M_t for p, ^{3}He, and α projectiles, except for the alpha particle incidence on lead. This can be explained from the fact that the low energy neutron production is greater in a heavier nucleus like lead because of its lower nuclear temperature.

C. Photon energy spectra and angular distributions

The photon energy spectra $\phi_\gamma(E,\theta)$ of carbon, copper, and lead targets at emission angles of $\theta=0$, 15, 45, 75, and 135 deg, normalized to one incident particle, are shown with their standard deviations for 33-MeV deuteron, 65-MeV ^{3}He, and 65-MeV alpha beams in Figs. 10, 11, and 12, respectively. The photon energy spectra were unfolded by Eq. (1), using a broad window function to the NE-213 scintillator, in order to suppress the oscillation of no physical meaning in the high energy region, and as a result the unfolded spectra in Figs. 10—12 have rather poor energy resolution. These figures reveal the following two facts:

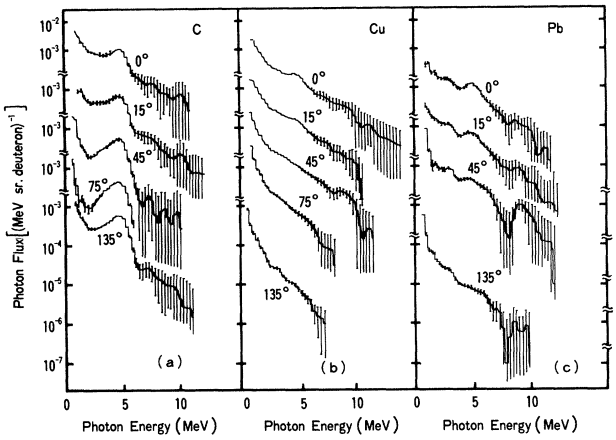

FIG. 10. Photon spectra of carbon, copper, and lead targets for 33-MeV deuteron injection at emission angles of 0, 15, 45, 75, and 135 deg. The spectra are normalized to one incident deuteron with a standard deviation.

(i) Since photons are mostly emitted isotropically from the excited states of the compound nucleus, the photon energy spectra are similar to each other at all emission angles for different combinations of projectile and target nuclei.

(ii) For the carbon target, the 4.43-MeV peak of photons emitted from the first excited state of ^{12}C due to the $^{12}C(i,i')^{12}C^*$ reaction is remarkable, where i means the incident particle of d, ^{3}He, and α. Two peaks of 2.0 and 6.6 MeV of photons from the first and second excited states of ^{11}C due to the $^{12}C(i,i'n)^{11}C^*$ reaction can also be seen for the alpha particle incidence. For copper and lead targets, the photon energy spectra are continuous with no remarkable peak due to dense excited states of compound nuclei.

The normalized angular distributions of the photon flux

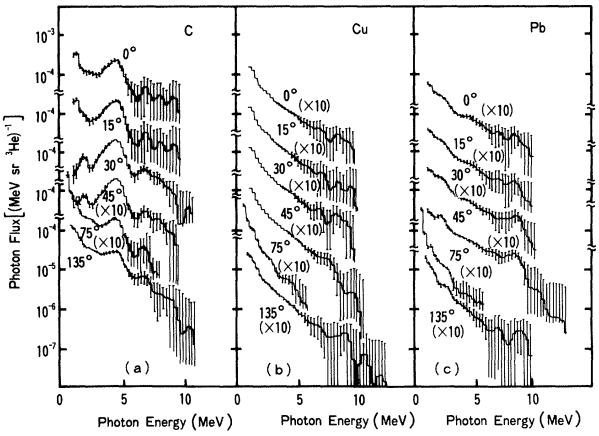

FIG. 11. Photon spectra of carbon, copper, and lead targets for 65-MeV ^{3}He injection at emission angles of 0, 15, 45, 75, and 135 deg. The spectra are normalized to one incident ^{3}He with a standard deviation. The number in the bracket means that the spectrum in the figure should be multiplied by it.

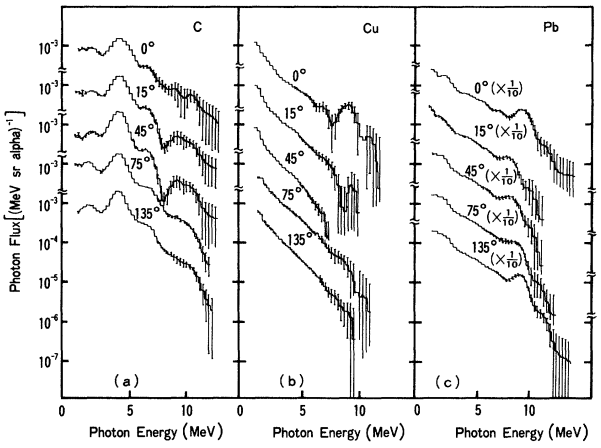

FIG. 12. Photon spectra of carbon, copper, and lead targets for 65-MeV alpha particle injection at emission angles of 0, 15, 45, 75, and 135 deg. The spectra are normalized to one incident alpha with a standard deviation. The number in the bracket means that the spectrum in the figure should be multiplied by it.

of Figs. 10–12 integrated over energy for carbon, iron, copper, and lead targets,

$$\phi_\gamma(\theta)=\int_{E_{\rm cut}}^{E_0}\phi_\gamma(E,\theta)dE\ , \tag{7}$$

are shown in Fig. 13, where $E_{\rm cut}$ is fixed to be 1.5 MeV for photons. The $\phi_\gamma(75)$ value for the deuteron incident on lead was as well estimated by the smooth interpolation of $\phi_\gamma(\theta)$ values at other emission angles as in the case of neutrons. The figure clearly shows that the photon angular distributions are much more isotropic than the neutron ones for all projectile and target combinations. This confirmed the idea that the photons are mostly emitted isotropically from a compound nucleus.

The photon yield, $Y_\gamma^{\rm tot}$, of energy above 1.5 MeV was obtained as

$$Y_\gamma^{\rm tot}=\int_0^\pi 2\pi\sin\theta\phi_\gamma(\theta)d\theta\ , \tag{8}$$

and is shown in Table II. From Table II, it is concluded that the photon yield, $Y_\gamma^{\rm tot}$ is the largest for the iron target, except for the deuterons on the carbon target, and decreases towards lead, and that the photon yields above 1.5 MeV are about 2–3 times larger than the fast neutron yields above 4 MeV, except for the protons and deuterons on the carbon targets, but are almost comparable to the total neutron yields, except for the protons on the carbon and lead targets. The decrease of $Y_\gamma^{\rm tot}$ on lead can be explained from the fact that the photons produced from lead have more components of energy below 1.5 MeV because of dense excited levels of the compound nucleus.

IV. COMPARISON WITH CASCADE MONTE CARLO CALCULATION

A. Method of calculation

The experimental results were analyzed by the LHI code programmed by Armstrong and Colborn.[11] The LHI

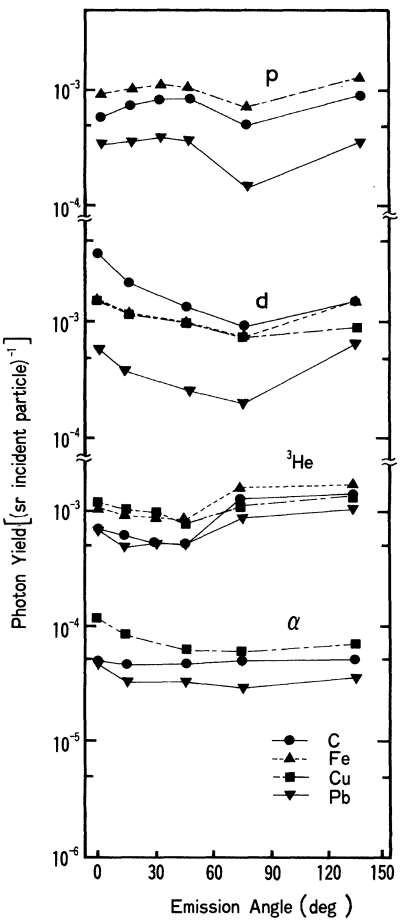

FIG. 13. Angular distributions of photon fluxes integrated above 1.5 MeV for proton, deuteron, ^{3}He, and alpha particle incidences on carbon, iron, copper, and lead targets.

transport code was made to predict radiation fields and effects produced in thick targets by light heavy-ion (LHI) beams, i.e., deuteron, triton, ^{3}He, and alpha beams by the Monte Carlo method, which was the extension of the HETC transport code[16] for proton, neutron, charged pion, and muon beams. The LHI code treats nonelastic nuclear collisions in LHI interactions with target nuclei by using the same intranuclear-cascade evaporation model as in the MECC-7 code.[10]

The basic assumption of LHI interactions is that the nucleons of the projectile LHI enter the nucleus separately and independently, except for their relative spatial locations when they enter the nucleus, with each nucleon having a kinetic energy $E_{\rm N}$ as

$$E_{\rm N}=(E_0-E_B)/M_p\ , \tag{9}$$

where E_0, E_B, and M_p are the kinetic energy, binding energy, and mass number of the projectile ion, respectively. According to Armstrong and Colborn,[11] this model has been found to give reasonably good agreement with experimental results for a projectile energy E_0/M_p between about 15 MeV/nucleon and a few GeV/nucleon and relatively light ions ($M_p \lesssim 4$) and relatively heavy target nuclei ($M_t \gtrsim 10$). They give the lower projectile energy limit, $E_0^{\rm min}$, of validity of the LHI code to be 32.2 MeV (16.1

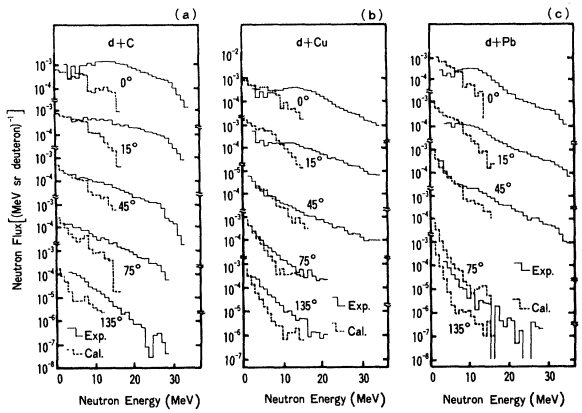

FIG. 14. Comparison of our experimental energy spectra of neutrons emitted from thick targets of carbon, copper, and lead exposed to a 33-MeV deuteron beam with those calculated by the LHI code.

MeV/nucleon) for the deuterons, 52.7 MeV (17.6 MeV/nucleon) for ^{3}He, and 88.3 MeV (22.1 MeV/nucleon) for the alpha particles. Here in our experiment, the 65-MeV alpha beam has rather lower energy than the beams above 88.3 MeV, so the neutron energy spectra produced by the 33-MeV deuteron and 65-MeV ^{3}He beams were calculated by the LHI code to compare with the experimental results.

In advance of this analysis, the variation of the total yield of neutrons produced was investigated by changing the cutoff energy E_c for nuclear interactions from the average nuclear potential B_N, i.e., the binding energy of a nucleon in the nucleus which is fixed to be 7 MeV in the LHI code up to 15 MeV to be used in the usual LHI calculation. In these low projectile energies close to $E_0^{\min}$, the calculated total neutron yield increased slowly with decreasing E_c and rapidly increased near B_N. As a result, the value of $E_c = 8$ MeV was selected for use in the LHI calculation.

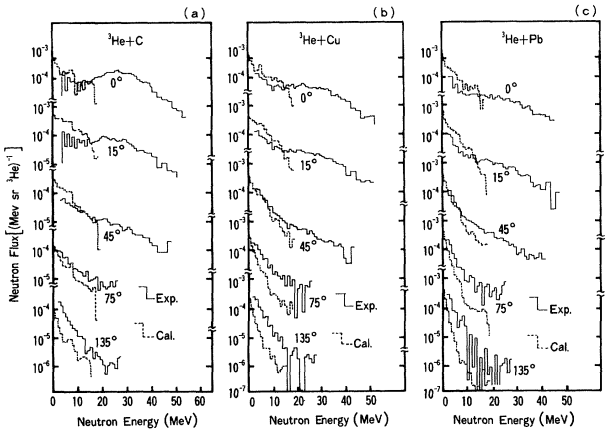

FIG. 15. Comparison of our experimental energy spectra of neutrons emitted from thick targets of carbon, copper, and lead exposed to 65-MeV ^{3}He beam with those calculated by the LHI code.

TABLE III. Measuring angles and corresponding angular intervals of the calculation.

Measuring angle	Angular interval of calculation
0°	0.5°– 7.5°
15°	7.5°– 22.5°
45°	37.5°– 60°
75°	60° – 90°
135°	120° –180°

B. Comparison with experimental results

Figures 14 and 15 show the comparison of our experimental energy spectra of neutrons emitted from thick targets of carbon, copper, and lead exposed by 33-MeV deuteron and 65-MeV ^{3}He beams, respectively, with those calculated by the LHI code. The angular intervals of the calculation corresponding to the experiment are shown in Table III. In order to compare with the experimental results at 0 deg, the angular interval of 0.5 to 7.5 deg was used in the calculation, because in the direction of 0 to 0.5 deg the uncollided nucleons of the projectile nucleons were stored as the emergent nucleons, and this calculational model gave an overestimation of the nucleon production. This exclusion of angles from 0 to 0.5 deg did not exert any noticeable influence on the estimate of the total neu-

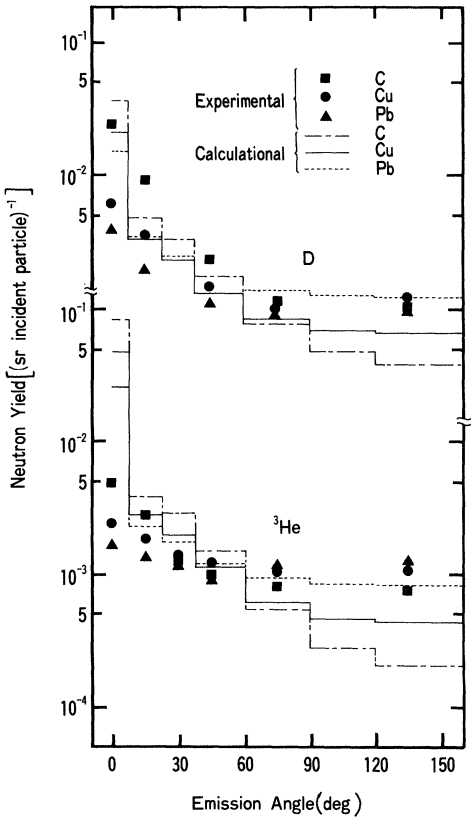

FIG. 16. Comparison of calculated and measured neutron angular distributions for thick targets of carbon, copper, and lead bombarded by 33-MeV deuteron and 65-MeV ^{3}He beams.

tron yield due to its very narrow angular interval.

From Figs. 14 and 15, the following facts can be seen. The calculated spectra are cut off at E_N in Eq. (9) and are quite different from the measured spectra at 0 and 15 deg, where the neutrons due to projectile splitting occupy a large fraction of secondary neutrons. The absolute values of the calculated spectra below about 10 MeV agree well with those of the measured spectra for the deuteron, but give a small overestimation for ^{3}He. At a large emission angle of 135 deg, the calculated spectra give a little softer spectra and an underestimation in absolute values compared with the measured spectra, and as a result, at 45 and 75 deg, the agreement between calculation and experiment is quite good in both spectral shape and absolute value. This discrepancy mainly comes from the Fermi free gas model which neglects the nucleon-nucleon coupling and treats nonelastic nucleon-nucleon interactions as a series of independent hadron-hadron collisions.

The calculated neutron spectra in Figs. 14 and 15 were integrated over energy at each emission angle and compared with the measured results $Y_n(\theta)$ in Eq. (6). Figure 16 shows the comparison of calculated and measured neutron angular distributions for thick targets of carbon, copper, and lead bombarded by 33-MeV deuteron and 65-MeV ^{3}He beams. The calculated results give sharper forwardness than the experimental results, but except at 0 deg, the agreement between calculated and experimental angular distributions is much better than the agreement between calculated and experimental spectra, because of better agreement of both spectra in the low energy region, where they have larger absolute values.

The calculated neutron angular distributions shown in Fig. 16 were integrated over angle to get the total neutron yields. The comparison of calculated and experimental total neutron yields, Y_n^{tot}, is shown in Table II. From the table, it is seen that the calculated results are in agreement with the experimental results within about 30%, except for the deuterons on the carbon target. Considering that the LHI code uses the rough model neglecting the nuclear structure and that the projectile energies in our experiment are fairly close to the lower energy limit of the validity of the LHI code, it can be concluded that the LHI code gives a good estimation of the total yield of neutrons produced by light heavy ions of low energy near 15 MeV/nucleon. (These calculations were performed with the FACOM M-180 II/AD computer of the Institute for Nuclear Study at the University of Tokyo.)

ACKNOWLEDGMENTS

The authors wish to heartily thank Dr. T. W. Armstrong and Ms. B. Colborn for giving us the LHI code in the development stage and allowing us to use it. The authors are also very grateful to Mr. K. Chiba for his helpful cooperation in running the LHI code. Many thanks are given to the machine group for operating the SF cyclotron.

*Present address: Mitsubishi Atomic Power Industries Co. Ltd., Shiba Park, 2-4-1, Minato-ku, Tokyo, Japan.

†Present address: Nippon Atomic Industry Group Co. Ltd., NAIG Nuclear Research Laboratory, Ukishima, 4-1, Kawasaki, Kanagawa, Japan.

[1]T. Nakamura *et al.*, Bibliography of Published Papers on Neutron and Photon Emission from Thick or Thin Target Bombarded by Charged Particles, Institute for Nuclear Study, University of Tokyo, Report INS-TS-20, 1981.

[2]A. Fasso and M. Höfert, Nucl. Instrum. Methods 133, 213 (1976).

[3]K. A. Weaver, J. D. Anderson, H. H. Barschall, and J. C. Davis, Nucl. Sci. Eng. 52, 35 (1973).

[4]J. P. Meulders, P. Leleux, P. C. Macq, and C. Pirart, Phys. Med. Biol. 20, 235 (1975).

[5]R. L. Macklin and J. H. Gibbons, Nucl. Sci. Eng. 31, 343 (1968).

[6]H. W. Patterson and R. H. Thomas, *Accelerator Health Physics* (Academic, New York and London, 1973), p. 141.

[7]P. H. Stelson and F. K. McGowan, Phys. Rev. 133, B911 (1964).

[8]T. Nakamura, M. Yoshida, and K. Shin, Nucl. Instrum. Methods 151, 493 (1978).

[9]T. Nakamura, M. Fujii, and K. Shin, Nucl. Sci. Eng. 83, 444 (1983).

[10]RSIC Computer Code Collection, Documentation for CCC-156/MECC-7 Code Package—Medium Energy Intranuclear Cascade Code System, Radiation Shielding Information Center, Oak Ridge National Laboratory, 1973.

[11]T. W. Armstrong and B. L. Colborn, Nucl. Instrum. Methods 169, 161 (1980).

[12]K. Shin, Y. Uwamino, and T. Hyodo, Nucl. Technol. 53, 78 (1981).

[13]Y. Uwamino, K. Shin, M. Fujii, and T. Nakamura, Nucl. Instrum. Methods 204, 179 (1982).

[14]K. Shin, Y. Hayashida, S. Shiroya, and T. Hyodo, J. Nucl. Sci. Technol. 16, 390 (1979).

[15]R. A. Cecil, B. D. Anderson, A. R. Baldwin, R. Madey, A. Galonsky, P. Miller, L. Young, and F. M. Waterman, Phys. Rev. C 21, 2471 (1980).

[16]T. W. Armstrong and K. C. Chandler, Nucl. Sci. Eng. 49, 110 (1972).